Nanoscale

PAPER

View Article Online
View Journal | View Issue

Cite this: *Nanoscale*, 2019, **11**, 16868

On the structure and chemistry of iron oxide cores in human heart and human spleen ferritins using graphene liquid cell electron microscopy†

Surya Narayanan,‡[a] Emre Firlar, ‡[a,b,d] Md Golam Rasul,[b] Tara Foroozan,[b] Nasim Farajpour,[c] Leigha Covnot,[a] Reza Shahbazian-Yassar *[b] and Tolou Shokuhfar *[a]

Ferritin is a protein that regulates the iron ions in humans by storing them in the form of iron oxides. Despite extensive efforts to understand the ferritin iron oxide structures, it is still not clear how ferritin proteins with a distinct light (L) and heavy (H) chain subunit ratio impact the biomineralization process. *In situ* graphene liquid cell-transmission electron microscopy (GLC-TEM) provides an indispensable platform to study the atomic structure of ferritin mineral cores in their native liquid environment. In this study, we report differences in the iron oxide formation in human spleen ferritins (HSFs) and human heart ferritins (HHFs) using *in situ* GLC-TEM. Scanning transmission electron microscopy (STEM) along with selected area electron diffraction (SAED) of the mineral core and electron energy loss spectroscopy (EELS) analyses enabled the visualization of morphologies, crystal structures and the chemistry of iron oxide cores in HSFs and HHFs. Our study revealed the presence of metastable ferrihydrite ($5Fe_2O_3{\cdot}9H_2O$) as a dominant phase in hydrated HSFs and HHFs, while a stable hematite (α-Fe_2O_3) phase predominated in non-hydrated HSFs and HHFs. In addition, a higher Fe^{3+}/Fe^{2+} ratio was found in HHFs in comparison with HSFs. This study provides new understanding on iron-oxide phases that exist in hydrated ferritin proteins from different human organs. Such new insights are needed to map ferritin biomineralization pathways and possible correlations with various iron-related disorders in humans.

Received 19th February 2019,
Accepted 17th August 2019

DOI: 10.1039/c9nr01541h

rsc.li/nanoscale

Introduction

Ferritins are globular protein shells with an 8 nm cavity inside capable of storing a few thousands of iron ions to form iron oxide core crystal structures.[1] In order to better understand the mineral core structure and kinetics involved in iron regulation, many groups employed bulk characterization techniques such as X-ray diffraction (XRD),[2] Mössbauer spectroscopy,[3] small angle X-ray scattering (SAXS),[4] X-ray near edge spectroscopy (XANES),[4] superconducting quantum interference device (SQUID),[4] and X-ray absorption spectroscopy (XAS).[5] These techniques, however, lack sufficient spatial resolution to probe the local chemistry and atomic order at the scale of individual ferritin proteins particularly within a liquid environment.[6]

Transmission electron microscopy (TEM) is a powerful characterization technique to study the structure and chemistry of the iron mineral core of ferritin at the nanoscale.[4,7–12] Most studies of the ferritin structure have been performed in a non-hydrated state where the ferritins were dried before imaging in TEM. Based on the electron nanodiffraction studies[8,13] and high-resolution transmission electron microscopy (HRTEM)[8] of physiological horse spleen ferritins (HoSFs),[8,13] human liver ferritins (HLFs),[8] and human brain ferritins (HBFs),[8] it was reported that all the ferritin types are composed of major phases of hexagonal 6-line ferrihydrite (6LFh) and hematite, with traces of magnetite (Fe_3O_4) or maghemite (γ-Fe_2O_3).[8,13] Conversely, pathological ferritin from HBF indicated the minor phases of 6LFh and the absence of hematite; however, the dominant phase was cubic magnetite.[8] Furthermore, based on HRTEM,[14] electron energy loss spectroscopy (EELS),[14] and microdiffraction studies,[15] Quintana *et al.* reported that the crystal structure of physiological HoSF exhibited 6LFh[14] and hematite as a major phase.[15] In contrast,

[a]*University of Illinois at Chicago, Department of Bioengineering, Chicago, IL, 60607, USA. E-mail: tolou@uic.edu*
[b]*University of Illinois at Chicago, Department of Mechanical and Industrial Engineering, Chicago, IL, 60607, USA. E-mail: rsyassar@uic.edu*
[c]*University of Illinois at Chicago, Department of Electrical and Computer Engineering, Chicago, IL, 60607, USA*
[d]*Institute for Quantitative Biomedicine, Rutgers University, Piscataway, NJ, 08854, USA*

†Electronic supplementary information (ESI) available. See DOI: 10.1039/c9nr01541h

‡Equal contribution; co-first authors.

pathological HBF was composed of major phases of magnetite and traces of ferrihydrite.[14] They also observed highly disordered stacking of oxygen and iron ions.[8] Galvez *et al.* also observed HoSF exhibiting different iron oxide phases during the stages of the demineralization process.[4] It is interesting to note that the composition of each phase of iron oxide was dependent on the stages of iron removal.[4]

In contrast to the results reported by Cowley *et al.*,[13] Quintana *et al.*[8,14,15] and Galvez *et al.*,[4] Pan and his co-workers showed that the iron core in HLF is made of single iron oxide phase 6LFh.[9] Through several[10,16,17] electron beam irradiation experiments on human liver biopsy, it was shown that under intense electron beam, iron oxide transformations might occur due to the shift of Fe^{3+} ions from octahedral coordinated sites to tetrahedral sites.[16] It was concluded that the earlier observation of magnetite/maghemite phases might be a consequence of electron beam irradiation.[9]

While the studies discussed thus far have improved the understanding of the structural aspects in ferritin proteins, the reported results are not consistent. The ambiguities surrounding iron core oxide phases, composition, and their relationship with the protein molecular structure call for more detailed investigation of ferritin proteins in their native state. The small size of the iron core and the difficulties associated with imaging of ferritin in its native hydrated environment might pose difficulties in understanding the iron oxide composition in ferritin.

With conventional protein specimen preparation for electron microscopy, artifacts could be introduced.[18] The evolution of electron cryomicroscopy (CryoEM) enabled the visualization of ferritin in a frozen state;[19] however, it has a major limitation to capture the dynamics of biomineralization pathways. The development of microfluidic-based liquid cell enclosures with Si_3N_4 membranes for TEM has opened a new avenue to study biological structures.[20] This development enabled us to resolve structural features and dynamics of COS-7 cells,[21] tumor cells,[22] yeast cells,[23] and other biological materials.[24,25] Furthermore, dynamic TEM (dTEM) was coupled with *in situ* Si_3N_4 based liquid microscopy to improve the spatial and temporal resolution, such that the conformational dynamics of the ferritin proteins could be observed.[26] While the dTEM technique has inheritably low resolution, it should be noted that the thickness of the Si_3N_4 membrane makes it difficult to obtain lattice resolution images of the iron-oxide mineral cores within ferritins.[27]

On the other hand, a graphene-liquid cell (GLC) has revolutionized our ability to resolve the atomic structure and chemistry at unprecedented resolutions. Yuk *et al.* developed this technique and observed the dynamics of Pt nanoparticle growth.[28] Furthermore, Wang *et al.* pioneered the atomic resolution characterization of HoSF in GLCs[18] and the precise control of electron beam to induce hydrogen molecule formation during GLC-scanning TEM (STEM) studies.[29] The superb electrical conductivity of graphene and its ability to scavenge free radicals make it a suitable candidate to image and analyse radiation sensitive biological materials in their native liquid environment.[30]

As reported in our earlier study on HoSF, the chemical signature of the iron oxide core in hydrated ferritin proteins is significantly different from the ferritins in the non-hydrated state. In particular, the EELS study from hydrated HoSF ferritin showed higher ratios of Fe^{2+}/Fe^{3+} in the mineral core as compared to the non-hydrated ferritins.[18] As such, it is important to investigate the iron core of ferritins in their native environment. Herein, we utilized GLC-STEM to characterize the iron oxide core minerals in different organ ferritins (human heart and human spleen) with varying ratios of heavy (H) and light (L) subunits. Through high angle-annular dark field (HAADF)-STEM imaging, the size and morphological characteristics of HSF and HHF were determined. The SAED and HRTEM analyses enabled the characterization of the crystal structure of HSF and HHF proteins. Furthermore, *via* the Fe $L_{2,3}$ edge analysis, the relative Fe^{3+}/Fe^{2+} ratios in the iron oxide cores of HSF and HHF in GLCs were compared.

Results and discussion

Morphology and size of ferritins

The morphology and the size differences of HSFs and HHFs are shown in Fig. 1. Fig. 1A shows the HAADF-STEM image collected from HSFs in GLCs exhibiting different morphologies with geometric and non-geometric shapes. The magnified images of the four particularly observed morphologies are depicted in Fig. 1B with their corresponding schematics: (i) full spherical, (ii) doughnut, (iii) trigonal pyramid, and (iv) crescent shapes. A similar trend was also observed in the HAADF-STEM images collected from HHFs as shown in Fig. 1C. Different morphologies observed in HHFs are also reported in the schematics along with the magnified images in Fig. 1D. In addition to the stick and boot like morphology that was discussed earlier by López-Castro *et al.*,[31] small spherical, bow-tie, crescent, and spherical morphologies were also observed in our work. Possible reasons can explain these different morphologies. (a) Periodic arrangement of iron crystals and stacking of various mineral cores in different sites and directions within the inner layer of the protein contribute to cubic symmetry.[1,32] Furthermore, the random orientation of the proteins on the support membrane results in different morphologies.[9] (b) The protein's inner architecture might dictate the growth of the iron oxide core thus exhibiting different morphologies.[33] (c) The nucleation sites, controlled by the number and positioning of the eight hydrophilic three fold symmetry channels determine the differences in morphology.[9] This theory is also supported by a model, called 24-n nucleation model, which describes the differences in the nucleation sites in HSFs and HHFs.[31] (d) The number of iron ions that enter the protein during the distinct stages of biomineralization, and the availability of iron ions for nucleation might contribute to different morphologies in HSFs and HHFs.[4,9,34]

In addition to the above-mentioned points, it is suggested that in a native form, both HSFs and HHFs can have a

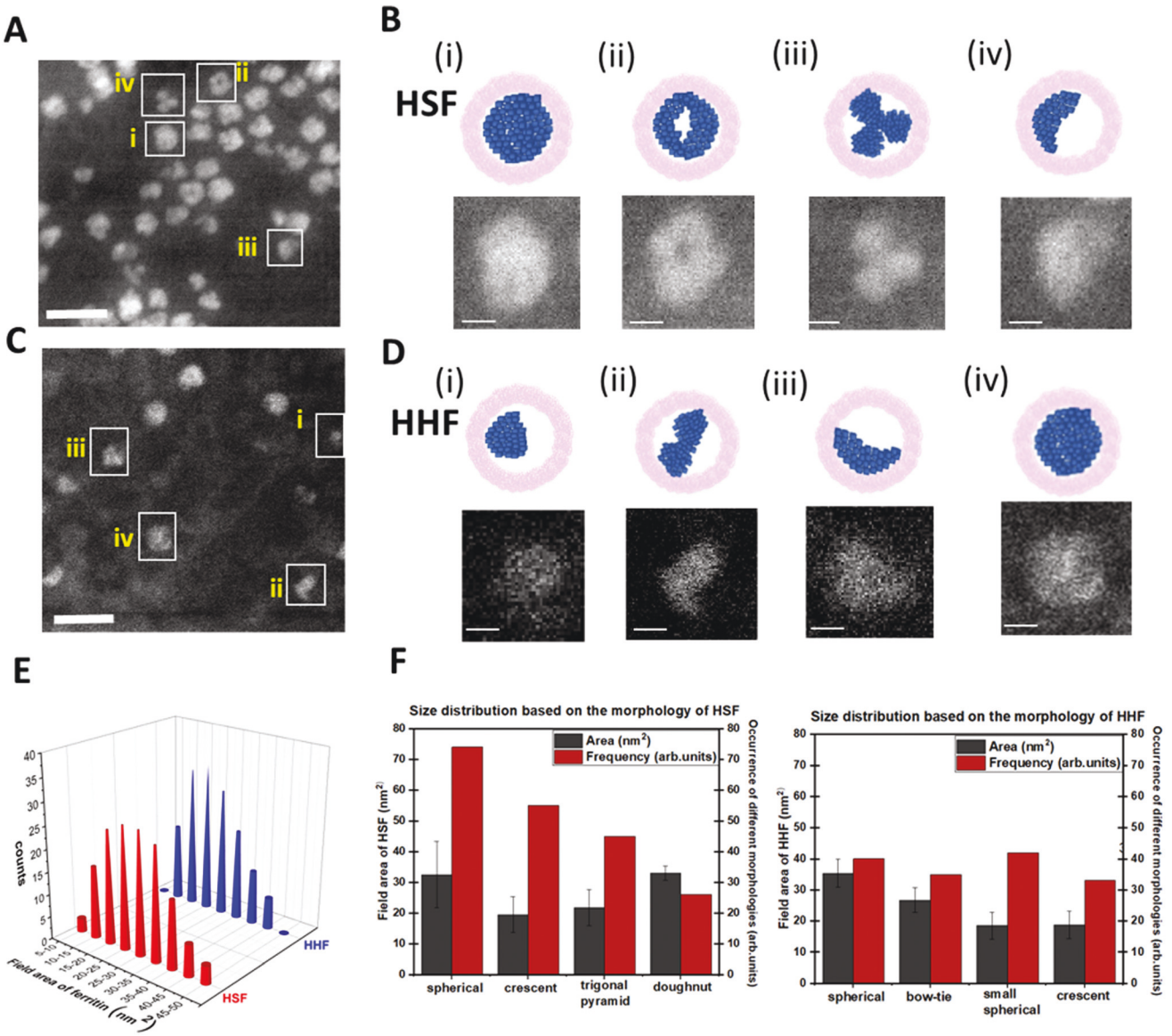

Fig. 1 Morphological characterization of HSF and HHF proteins in GLCs. (A) HAADF-STEM image of HSF in GLC showing different morphologies with geometric and non-geometric shapes (scale bar: 20 nm). (B) Magnified images of different geometric morphologies observed in (A) and their corresponding schematics representing the morphologies that are exhibited by HSF. The different morphologies depicted are: (i) full spherical, (ii) doughnut, (iii) trigonal pyramid and (iv) crescent (scale bar: 2 nm). The pink color represents the protein shell while the blue color represents the iron oxide core in ferritin. (C) The HAADF-STEM image of HHF in GLC showing different morphologies with geometric and non-geometric shapes (scale bar: 20 nm). (D) Magnified images of different geometric morphologies observed in (C) and their corresponding schematics representing the morphologies that are exhibited by HHF: (i) small spherical, (ii) bow-tie, (iii) crescent and (iv) spherical (scale bar: 2 nm). The pink color represents the protein shell while the blue color represents the iron oxide core in ferritin. (E) Size distribution of iron cores in HHF and HSF proteins based on the area of the particles in the HAADF-STEM images. The size distribution measurements showed 26 ± 9 nm^2 for HSF and 24 ± 8 nm^2 for HHF (n = 150 for each type of ferritin). (F) The size distribution measurements of HSF and HHF (n = 150 for each type of ferritin) with respect to different morphologies in HSF and HHF. This work focuses on the morphologies with geometrical shapes.

different distribution of H and L subunits.[1] The position and the number of H and L subunits might also have an impact on the morphologies that are exhibited in both HSFs and HHFs. In this study, HSFs were obtained from a native source while HHFs were obtained from a recombinant ferritin source. While a naturally available source of protein can exhibit different ratios of H/L subunits, studies have shown that the ratio of H and L subunits can be controlled in a recombinant protein structure.[35] Due to these differences in the source of protein, the number of morphologies that are observed in HHFs could be limited. Future studies can consider using HHF from a native source to discover some unique morphologies that are not reported in this work. Furthermore, it is shown that higher ratios of H/L subunits have an influence on the number of iron that enters the ferritin to form an iron oxide core, as well as the kinetics of biomineralization and

demineralization.[35] A previous study showed that with a fewer number of ferroxidase sites and slower oxidation rates, L rich ferritins tend to have a bigger iron oxide core with more pronounced crysallinity.[35] Fig. 1E represents the iron oxide core size distributions of HSF and HHF. The graph represents a bell curve of 150 different iron oxide cores for HSFs and HHFs with a similar particle size distribution. Since the iron oxide core shape is not spherical, area was considered for the size comparison. The average size distribution of HSFs was found to be 26 ± 9 nm^2 while for HHFs, this was slightly lower (24 ± 8 nm^2). One reason behind that could be the slow mineralization in the L subunit rich ferritins, HSF, as is also reported in the literature.[36] The area of the iron oxide core within ferritins was analyzed based on the morphologies as shown in Fig. 1F. The bar chart represents the area (black color) and frequency (red color) of HSFs and HHFs. HSFs displayed a higher frequency of spherical (32.5 ± 10.8 nm^2) morphologies as compared to the crescent (19.48 ± 5.8 nm^2), trigonal pyramid (21.74 ± 5.8 nm^2), and doughnut (32.97 ± 2.3 nm^2) morphologies. On the other hand, the distribution of crescent (18.75 ± 4.4 nm^2), small spherical (18.47 ± 4.2 nm^2), bow-tie (26.72 ± 3.88 nm^2), and spherical (35.34 ± 4.5 nm^2) morphologies in HHFs did not follow a trend. The frequency of occurrence of different morphologies might be a representation of different stages of biomineralization.[9] There is also a possibility that it indicates the role of H and L subunits in HSF and HHF during the nucleation and growth of the minerals.[31] It should be noted that the sample dataset is not comparable with the ones used typically in the cryo-EM community. Considering the randomness of graphene liquid pockets across the grid, it is challenging to incorporate a high-throughput automated data collection system to collect large datasets.

Structural characterization of ferritins

Fig. 2 represents the structural characterization of HSFs and HHFs using SAED and high resolution TEM (HR-TEM) techniques. The SAED analysis (n > 6 for both types of ferritins) was carried out to determine the average crystal structure of many different ferritin cores from a selected area in the liquid state, while HR-TEM was employed to monitor the crystal structure of individual protein mineral cores in the non-

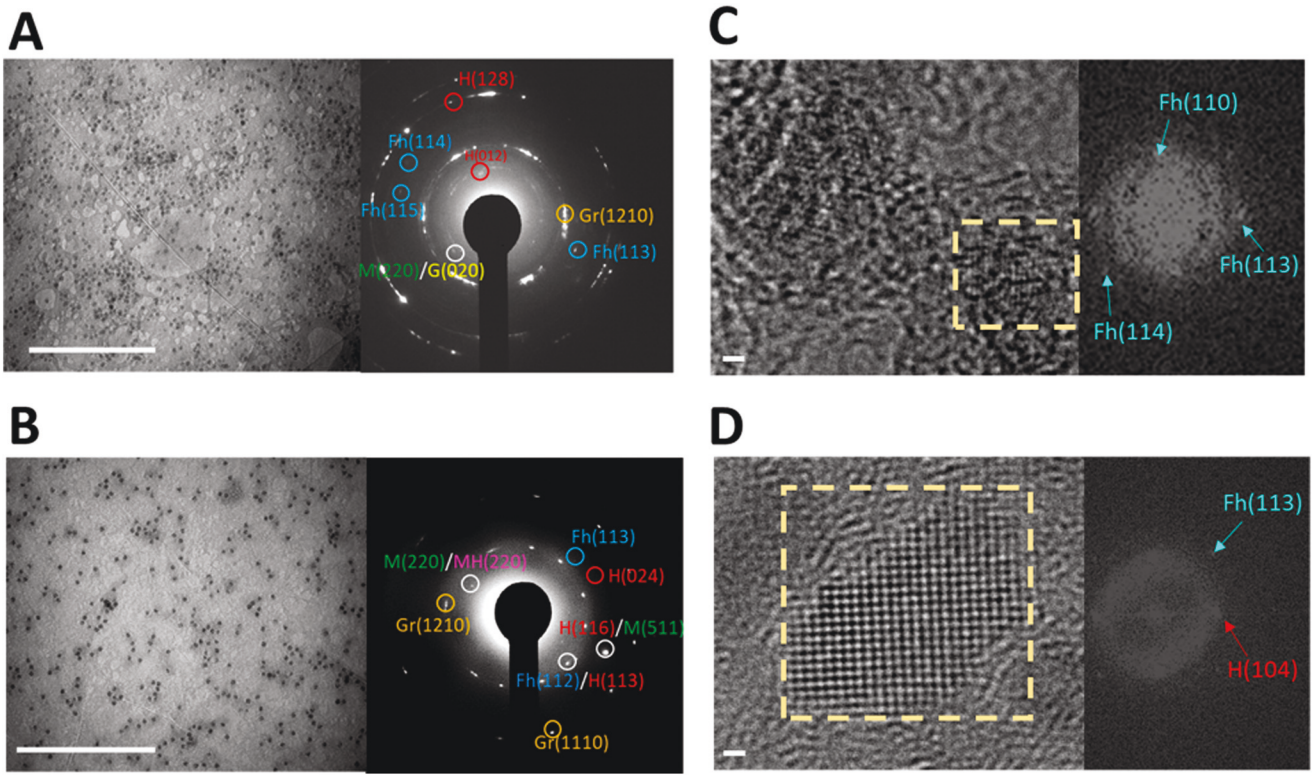

Fig. 2 Electron microscopy characterization of HSF and HHF proteins. (A) TEM image and the corresponding SAED of HSF indicate d spacings of 3.5, 3.1, 1.9, 1.7, 1.5 and 1.1 Å representing crystal structures with planes H(012), M(220) or G(020), Fh(113), Fh(114), Fh(115) and H(128), respectively. The d spacing of graphene of 1.2 Å is represented as Gr(1210). (B) TEM image and the corresponding SAED of HHF indicate d spacings of 3.0, 2.2, 2.0, 1.8, and 1.6 Å representing crystal structures with planes M(220) or MH(220), Fh(112) or H(113), Fh(113), H(024), and H(116) or M(511), respectively. The d spacings of 2.1 and 1.2 Å represent Gr(1100) and Gr(1210), respectively. Green, blue, yellow, red, pink and gold colors in the SAED represent magnetite (M), ferrihydrite (Fh), goethite (G), hematite (H), maghemite (MH) and graphene, respectively. Scale bars of the TEM images in (A) and (B) are 100 nm. (C) HR-TEM image of HSF with the FFT obtained from the dashed square (yellow color) area of the image. Interplanar spacings of 2.4, 1.97, and 1.49 Å in the FFT refer to the (110), (114) and (113) planes of ferrihydrite, respectively. (D) HR-TEM image of HHF with the FFT obtained from the dashed square (yellow color) area of the image. Interplanar spacings of 2.7 and 1.9 Å in the FFT refer to the (104) plane of hematite and the (113) plane of ferrihydrite, respectively. Scale bars of HR-TEM images in (C) and (D) are 2 nm.

hydrated state. Fig. 2A shows both the reference TEM image and SAED collected from an area where multiple HSF particles are present. The *d* spacings of 3.5, 3.1, 1.9, 1.7, 1.5, and 1.1 Å indicate the presence of hematite (H), ferrihydrite (Fh), and traces of goethite or magnetite with the planes of H(012), M(220)/G(020), Fh(113), Fh(114), Fh(115) and H(128), respectively. Quintana *et al.* also showed the presence of ferrihydrite and hematite for HSF through dry state HR-TEM.[8] Fig. 2B, on the other hand, represents the reference TEM image and SAED collected from an area where multiple HHF particles are present. SAED patterns showed *d* spacings of 3.0, 2.2, 2.0, 1.8, and 1.6 Å, which indicate the presence of hematite, ferrihydrite, and traces of magnetite or maghemite with the planes of M(220)/MH(220), Fh(112) or H(113), Fh(113), H(024), and H(116) or MH(511), respectively.

Considering these, HSF and HHF showed similar crystal structures indicating the presence of ferrihydrite as a predominant phase along with hematite. In addition to that, some of the *d* spacings from HSF also matched with the planes of magnetite as well as goethite. On the other hand, HHF indicated trace amounts of magnetite/maghemite. To be able to study the individual crystal structures, furthermore, HR-TEM images were collected from HSF and HHF and presented in Fig. 2C and D, respectively. Their corresponding Fast Fourier Transforms (FFT) showed interplanar spacings of 2.4, 1.97, and 1.49 Å representing ferrihydrite with planes (110), (114) and (113) for HSF, respectively, in Fig. 2C, and 2.7, and 1.9 Å representing hematite with plane (104) and ferrihydrite with plane (113) for HHF, respectively, in Fig. 2D.[37] HR-TEM does not represent all the iron oxide minerals reported *via* SAED because not all the crystals in the mineral core are in the right crystallographic zone axis. Hence, the planes of goethite, magnetite, and hematite were not observed in HSF. Likewise, the planes of maghemite and magnetite were not observed in HHF from the HR-TEM images.

Chemical characterization of ferritins

The ability to acquire EELS maps at 10^6 e^- $Å^{-2}$ s^{-1} has showcased the ability of graphene to maintain the integrity of the protein structure in ferritin during high dose EELS signal collection.[18] In this work, the differences in the chemical composition of the mineral cores in HSF and HHF in their native state are investigated *via* GLC-STEM-EELS. White line analysis on iron L_3 and L_2 core edges was implemented for the determination of the oxidation state of transition metals.[38,40,42] It was reported that with the increasing area integral ratio of L_3 to L_2, the oxygen to transition metal ratio increases.[39] This technique was also employed here to determine the relative ratio of O to Fe, which, in turn, also indicates the variation in the Fe^{3+} to Fe^{2+} ratio. Fig. 3A represents the iron L_3 and L_2 edges obtained from HSF and HHF (n = 3 for both the ferritin types). Comparing the integral intensities under these white lines, the L_3/L_2 ratios are 4.24 ± 0.06 for HSF and 4.53 ± 0.04 for HHF, as shown in Fig. 3B. These results were compared with the magnetite and hematite standards which indicated that as this ratio increases, the ratio of O/Fe or Fe^{3+}/Fe^{2+} increases.[40]

Scheme 1 represents the differences in the iron oxide composition in HSF and HHF based on our observation reported here. Diffraction patterns from hydrated HSFs and HHFs indicated higher amounts of ferrihydrite in comparison with other phases of iron oxide in both HSFs and HHFs. In addition to that, some amount of hematite was observed in both the organ ferritins. Generally, ferrihydrite[19] forms at the early stage of the biomineralization process. Although ferrihydrite is a labile form of crystal, it is present in ferritin due to its ability to

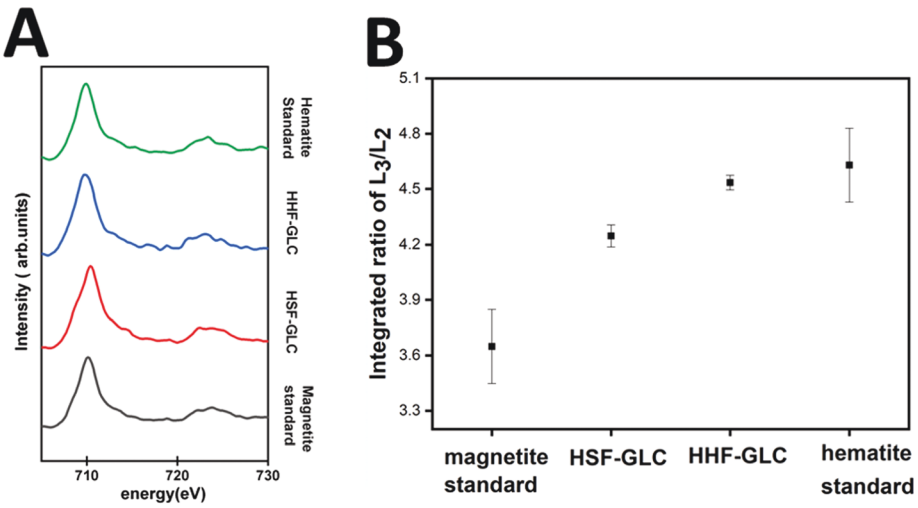

Fig. 3 Chemical characterization of HSF and HHF *via* GLC-STEM-EELS. Chemical characterization of HSF and HHF. (A) STEM-EELS in GLC shows the comparison of Fe $L_{2,3}$ edges in HSF and HHF iron cores with the iron oxide standards. (B) Relative area integral ratio of $L_3$to L_2 Fe edges in HSF and HHF. The higher ratios in HHF (4.53 ± 0.04) as compared to HSF (4.24 ± 0.06) indicate higher O to Fe ratios, that is, the presence of higher amounts of Fe^{3+}/Fe^{2+} in HHF as compared to HSF (n = 3 for both the ferritin types). Magnetite (3.64 ± 0.2) and hematite (4.63 ± 0.2) standards (n = 3) are represented to draw an understanding of the Fe^{3+}/Fe^{2+} ratio.

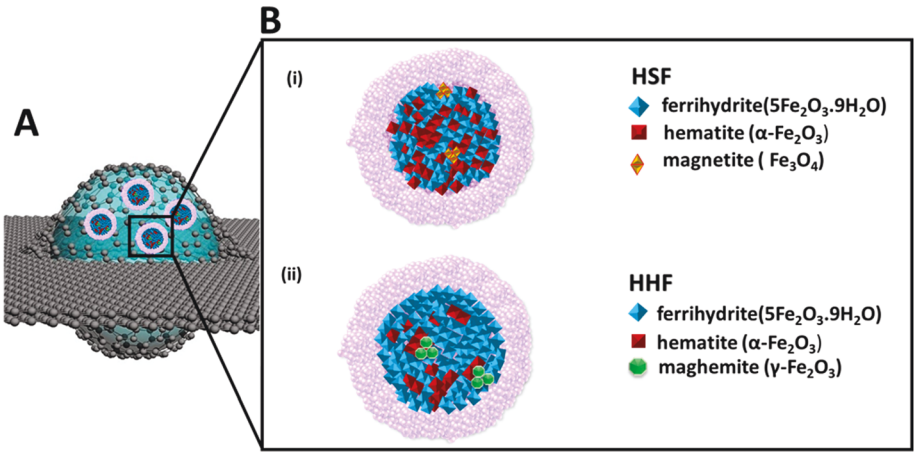

Scheme 1 Schematic showing the encapsulation of ferritin proteins within GLC capsules and the differences in the iron oxide phases of HSF and HHF. (A) Graphene liquid cell encapsulation allows imaging of ferritin proteins in their native liquid state. (B-i) HSF protein with the protein shell (pink color) and the iron mineral core composed of ferrihydrite (Fh), hematite (H), and the traces of magnetite (M). The percentage composition and location of Fh, H, and M are represented solely for schematic purpose. (B-ii) HHF protein with the iron mineral core composed of ferrihydrite (Fh), hematite (H) and maghemite (MH). The percentage composition and distribution of Fh, H, and MH are represented solely for schematic purpose.

demineralize faster than the other forms of iron oxide.[36] From a thermodynamic standpoint, formation of hematite is favoured from the ferrihydrite crystal structure.[41,42] However, the inner environment and the protein chemistry tend to retain the water molecules and influence the formation of selective crystal types.[36] In addition to ferrihydrite and hematite, traces of the magnetite phase were also observed in hydrated HSF, which was not evident in HHF. Although the *d* spacings can be matched with two different iron oxide types, it can be speculated that the crystal structure is closer to magnetite as the EELS results also indicated the higher ratios of Fe^{2+}/Fe^{3+} in HSF. The presence of magnetite in ferritin has also been supported by several electron microscopy[3,8,9,23] and non-EM[1,23,25–27,43–46] based experiments. Furthermore, a model for magnetization of ferritin[47] supported the presence of magnetite in ferritins. Biologically, the presence of magnetite could be related to the oxidation and precipitation of adsorbed ferrous ions on the surface of the ferrihydrite crystal core.[48] The diffraction patterns of wet HHF collected from different areas indicated the presence of magnetite or maghemite in addition to ferrihydrite and hematite. The EELS studies indicated higher ratios of Fe^{3+}/Fe^{2+} in comparison with HSF, because of which there is a higher probability of having maghemite instead of magnetite in HHF.

While it is less likely that the observation of magnetite in the wet state is due to the effect of electron beam irradiation since the same phenomenon was not observed in dry state ferritins, we believe further studies on the role of electron beam on this phenomenon are necessary. It is interesting to note that the types of iron oxides formed inside the protein shells are limited to the above-mentioned types. However in the absence of a protein shell, formation of akaganeite (β-FeO(OH),[49] goethite (γ-FeO(OH)) and lepidocrocite (α-FeO(OH))[36] is favoured based on the classical nucleation theory. The surface energy due the larger surface to volume ratio of the mineral core can contribute to the thermodynamic stability of the nanosized crystals.[36]

GLC-STEM-EELS white line analysis showed a higher ratio of Fe/O, thus higher Fe^{3+}/Fe^{2+} in HHF compared to HSF. This observation could be due to several possibilities: (1) The ability of HSF to apprehend higher numbers of Fe^{2+} compared to HHF[35] could result in the nucleation of iron ions before the completion of iron oxidation from Fe^{2+} to Fe^{3+} form. (2) The metabolic state of the cells in the different organs.[50] (3) The presence of larger ratios of H/L subunits in HHF compared to HSF could affect the ratio of Fe^{3+}/Fe^{2+}.[35] After the ferrous iron internalization by ferritin through eight hydrophilic channels, the dinuclear ferroxidase sites, which are present in H subunits convert ferrous iron to ferric oxide species through the following reaction: $2Fe^{2+} + O_2 \rightarrow Fe^{3+}–O–O–Fe^{3+}$.

It should be noted that this is the first time the structural and chemical characterization of hydrated HSF and HHF is reported. There are some SAED and EELS studies that report the differences in H and L rich ferritins based on the conventional sample preparation for TEM studies (no cryoTEM).[4,8,9,51] However, there are discrepancies in the results that are previously reported. While some of the studies report that both H- and L-rich ferritins are composed of ferrihydrite,[9,51] there are also results which support the polyphasic nature of iron oxides.[4,8] Our results indicate that both HSF and HHF are polyphasic in nature, with iron oxide composites. While drying of the proteins is not desirable (in c-TEM), it is also possible that proteins are the victim of electron induced radiolysis in the absence of a protective graphene cover. Studies have shown that biological samples with a protective graphene cover were less prone to radiolysis even with a higher total dose compared to a threshold dose.[18,30,52] It should also be noted that the presence of buffers surrounding the protein might influence the pH of the solution by establishing an equilibrium between the oxidation and reduction processes.[53,54] While it is possible

to have the effect of buffer in the liquid environment, it becomes challenging to maintain the buffers during dry c-TEM imaging. This could possibly differentiate the results obtained *via* c-TEM *versus* the observation made *via* our GLC-TEM. It would be interesting to study the influence of solvents in the solution on maintaining an exceptionally high stability towards electron beam induced iron transformations. This could possibly differentiate the results obtained *via* c-TEM *versus* the observation made *via* our GLC-TEM.

Considering the need for a surrounding liquid environment to keep the protein structure intact,[55] the crystal structure and chemistry of HSF and HHF were evaluated in the liquid state. Furthermore, to understand the differences in the composition of the protein in the native wet environment and the dry state results reported in the literature,[9,16] the same analysis was carried out in the absence of liquid. The results obtained from the dry state ferritin indicated the predominant hematite phase with some ferrihydrite,[4] in addition to the traces of goethite or magnetite (Fig. S1†). It is reported that the loss of water favours the formation of hematite[42] which might be a reason to observe major phases of hematite in dry state diffraction studies. Furthermore, magnetite was observed only in the wet state HHF diffraction analysis. It should be noted that there has also been a lack of reports on characterization studies on the iron oxide mineral type in the HHF core in the literature, thus, the comparison of the wet and dry results with the dry state reports from the literature was limited to HSF. To comprehend the differences between the dry and wet state in terms of O to Fe ratio, EELS was also carried out in both states and it was observed that the ratio in wet state HSF is higher than dry state HSF (Fig. S2†). In addition to that, a sharp pre edge feature at 709.2 eV and an edge at 710.7 eV with a difference of 1.5 eV were observed in the dry state which can be inferred as hematite.[56] The pre edge was not prominent in the wet state which might be due to the scant amount of hematite in the wet state compared to the dry conditions. The ferritin structure in the dry state might not be a true representation because of the TEM sample preparation techniques that can cause deviations from the native properties of biological samples. The loss of liquid after drop casting onto the TEM grid and further drying of the sample in the electron microscope chamber could be an additional factor affecting the protein structure. The role of graphene to keep the liquid layer intact around the protein shell has an impact on the integrity of the proteins. The hydrogen bonds hold the polypeptide bundles together in the presence of water and thus might have an impact on the iron oxides formed inside the protein. In the absence of water, the hydrogen bonds break down and the structural integrity of the protein shell surrounding the iron oxide core is lost.[55] Hence, the loss of protein will remove some of the contribution of oxygen from the shell, decreasing the O/Fe ratio, thus, the Fe^{3+}/Fe^{2+} ratio. While we noted the differences in L_3/L_2 ratio edges in wet and dry specimens, there is a small overlap pointing to the fact that statistical analysis should be performed on large datasets to fully analyze the trend in the L_3/L_2 ratio in wet and dry states.

We should also highlight that studying proteins in the liquid state has some advantages over the cryo-TEM technique: (1) due to the ability to keep the liquid surrounding the protein as one of the active components, the hydration forces of water at room temperature help maintain the stability of the proteins.[57] On the other hand, the cryo freezing of water not only increases the density of the protein artificially, but also impacts the inner cavity causing protein destabilization.[58] Studying proteins in liquid at room temperature will facilitate the protein stability. (2) Additionally, liquid-cell TEM allows the study of dynamics or structural transformation in proteins. (3) Furthermore, the GLC-TEM technique does not require costly cryo-TEM instrumentation or special TEM holders.

The effect of electron dose on the chemistry of ferritin was also considered in this study. The electron dose was rigorously controlled during imaging to minimize the effect of electron beam on determining the type of iron oxide crystal in ferritin cores. In fact, our earlier work has shown the strategy to control the chemical environment of GLCs.[29] The concentration of H_2 species during the electron beam irradiation is dependent on the electron dose rate (Fig. S3 and Video S1†).[59] This relationship can be given by the equation: $C_{H_2} = \alpha_i(10^5 \cdot S \cdot D_r)^{\beta_i}$, where C_{H_2} is the concentration of hydrogen species, S is the stopping power, α_i and β_i are constants, and D_r is the dose rate.[59] With a lower electron dose rate, the bubble formation and the generation of radiolysis species can be controlled as also reported by Wang *et al.*[29] This is because the radiolysis products increase exponentially at the onset of electron beam irradiation. However, an equilibrium is established over time due to the annihilation reaction between the primary radiolysis products and water.[29] This effect establishes a direct relationship between the electron dose rate and the formation of radiolysis products.[29] Future studies should incorporate the effect of dose *vs.* dose rate while studying the iron oxides in ferritin.

Furthermore, in the same work, it was shown that the internal pressure in the GLCs has a direct correlation with the threshold electron dose rate, given by the relation $p^2 \propto D_r$, where p is the pressure and D_r is the electron dose rate.[29] The experiments were designed taking the effect of electron dose rate into consideration (as also demonstrated in Fig. S4 and S5†). The electron dose calculation and the corresponding doses for different imaging and EELS experiments are reported in the Experimental procedure section. While the electron dose induced radiolysis products can influence the local environment facilitating the iron reduction process, it should be noted that besides the protective graphene cover, the proteins are surrounded by the buffered solution at pH 7.5. Studies have shown the influence of both the initial pH as well as the buffers affecting the local environment of the solution.[53] In deionized water, the effect of radiolysis species such as H_3O^+ ions is known to decrease the pH of the solution, thus influencing a reducing environment.[53] However, in the presence of buffered solution containing chloride ions, there is a possibility that the condition is

reversed, favoring an equilibrium state between the oxidation and reduction processes.[54] However the effect of preservatives such as bromo-nitro-dioxanes and methylsothiazolone is not well studied. It would be interesting to study the effect of these species in electron beam-induced transformations.

Pan and his coworkers[10] studied the composition of ferritin subjected to varied electron doses starting from 10^5 to 10^9 electrons per nm^2 electron dose in the dry state. They also reported that the Fe^{3+}/Fe^{2+} ratio of iron in hemosiderin and cytosolic ferritins (which was studied in this work as well) did not vary with the increase of total electron dose.[10] In our study, although the dose conditions were the same in both the types of ferritins, the chemical information obtained from HSF and HHF proteins were different indicating that the conclusions in this study are not influenced by the electron beam. The ability of using higher electron doses during GLC imaging compared to other low dose electron imaging setups could be attributed to the novel material properties of graphene: (i) graphene is a very good electronic conductor, eliminating further accumulation of incident electrons in the sample during electron imaging. Hence, sample charging and the resulting formation of radiolysis products were minimized.[60] (ii) Due to the lower total thickness of GLCs, the number of secondary electrons formed due to electron–sample interaction is lower than the relatively thicker Si_3N_4 based fluid cell setup.[61] (iii) In the event of radiolysis, the radicals form and graphene is also reported to be a good radical scavenger, which helps in the prevention of possible unwanted radical–sample interaction (also see the ESI†).[30] Due to these reasons, GLCs enable the utilization of higher electron doses in comparison with conventional TEM imaging of biological or beam-sensitive samples.

Conclusion

Graphene liquid cell-TEM imaging and spectroscopy were utilized to analyse the structural and chemical differences in the iron oxide cores of different organ ferritins. It is expected that the higher number of active sites in H subunits facilitates continuous oxidation and rapid biomineralization of iron oxides. Both HSF and HHF were observed to have ferrihydrite and hematite. However, the L- and H subunit rich ferritins also showed traces of magnetite and maghemite, respectively. Excess of iron ions that enter the protein might get deposited on the surface of the iron core crystal resulting in magnetite formation. Slow kinetics and incomplete biomineralization could also be other reasons for the observation of magnetite in HSF, and the higher rate of the reduction process can explain the observation of maghemite in HHF. Higher ratios of O/Fe or Fe^{3+}/Fe^{2+} were observed in HHF compared to HSF in the liquid state. This might be due to several factors which include the number of iron ions that are available for oxidation, the metabolic state of the cells in the organ, as well as the presence of larger ratios of H/L subunits causing ferroxidation in HHFs compared to HSFs. Future studies can focus on observing the biomineralization in real-time, which can further help understand the correlation between the chemical compositions of different iron oxides and the organ ferritins. It was also observed that the dried HSF contained a lower ratio of Fe^{3+}/Fe^{2+} as compared to the wet HSF. This is attributed to the degraded nature of air-dried ferritin resulting in the loss of oxygen from the ferritin shell that contributes to the Fe/O ratio. It should be noted that this study was limited to the characterization of crystalline iron oxides in HSF and HHF. Future studies should be considered to study the non-crystalline or partially crystalline forms of iron oxide in ferritin. The ability of GLC-TEM to image proteins under native wet conditions offers new opportunities in exploring the interaction of proteins and inorganic materials. Future directions will focus on observing the iron core growth and understanding the nucleation mechanism in ferritin using *in situ* liquid microscopy.

Experimental procedure

Materials

HSF (Catalog #270-50) and HHF (Catalog #FERT16-R-50) were purchased from Lee Biosolutions, USA and Alpha Diagnostics International, USA, respectively. The protein samples were diluted with 1× PBS buffer to 0.4 mg ml^{-1} for all the experiments.

Graphene grids

The grids used for the experiments are 300 mesh Au lacey carbon TEM grids (LC325) purchased from Electron Microscopy Sciences (EMS). A slightly modified protocol from that of Regan and his coauthors was followed.[62] The gold grids were placed on the in-house grown graphene coated copper sheets. The grids and the copper sheets were flattened and pressed against each other by applying gentle pressure through the lens paper. After that, 1 μl of IPA was added to the sides of the grid to attach the grid to the copper sheet. The gold grids on the copper sheet were air dried for 5 minutes to get rid of excess IPA. Then the grids were placed on the hot plate at 50 °C for 10 minutes. The copper sheet was placed in the $FeCl_3$ etchant for 3 hours. To prevent the silicon nanoparticles that would deposit from the silicon-based glass containers during etching, Nalgene containers were used for all the experiments. After 3 hours, the grids were washed with deionized water three times.

TEM sample preparation

The protein samples were drop-cast in the commercially available lacey carbon film coated copper grid (Catalog# LC300-CU, Electron Microscopy Sciences) and air-dried to collect the HR-TEM and SAED patterns. After that, the liquid protein samples were encapsulated in the graphene sandwiches as described by Wang *et al.*, (2014)[18] for STEM images and chemical characterization using STEM-EELS.

Sample characterization

STEM images were collected from GLC-TEM experiments and were processed with ImageJ to determine the size and morphology of the particles. The analysis was done for 70 different particles for each ferritin sample. The particle sizes were grouped with the bins of 5 nm^2. Then, the average area was calculated along with the frequency. To this end, the data set was plotted in Origin Pro (version: b9.4.0.220). The structural characterization of both the samples was analysed by measuring the interplanar distances in both GLC and the dry state *via* 80 kV Hitachi HT7700 at 80 kV and JEOL 3010 at 300 kV, respectively. HR-TEM images on the dry samples were collected using JEOL-JEM 3010 at 300 kV. GLC-TEM electron imaging and diffraction were collected with 1 second exposure using the electron dose range of 16 to 181 e $Å^{-2}$. Dry state TEM imaging and diffraction were collected with 0.1 second exposure. GLC-HAADF STEM imaging and chemical characterization were carried out using the probe aberration corrected JEOL-JEM 200CF operated at 80 keV. The microscope is equipped with a Cold Field Emission Gun and GIF Quantum EELS (Gatan, Inc., USA) that has a spatial resolution of 1.3 Å and an energy resolution of about 0.35 eV. For STEM imaging and EELS, a convergence semi angle of 22 and 17.8 mrad was used, respectively. For STEM images, a HAADF detector with an inner detection angle of 90 mrad was used for better Z contrast. Images were collected with 512 × 512 pixels and a dwell time of 31.2 μs. The video was collected in Ronchigram mode with 0.01 s per frame exposure time. For EELS, a collection angle of 53.4 mrad was used for better quality signals. The energy resolution was determined by measuring the full width at half maximum of the zero-loss peak and it was around 0.6 eV. The spectrum was acquired with the dispersion of 0.15 eV per channel with an exposure time of 0.1 s. The electron dose rates for HAADF imaging and EELS analysis were approximately 9 e $Å^{-2}$ s^{-1} and 7.2 × 10^6 e $Å^{-2}$ s^{-1}, respectively. Origin Pro[18] was used to calculate the integral white line intensities.

Data analysis

The interplanar distances were measured both *via* the FFT of the image in HR-TEM images and SAED patterns using DigitalMicrograph. SAED data were analysed using the DigitalMicrograph. For the EELS analysis, the background was subtracted using the 50 eV integration window in the DigitalMicrograph and the energy range was considered from 705 to 730 eV for the analysis.[63] The L_3 and the L_2 edges were normalized and the background was subtracted for plural scattering. Then, the related area integral ratio was calculated by fitting a Gaussian under the peaks using Origin Pro (version: b9.4.0.220).[40] A comparison figure of individual magnetite standard, HSF, HHF, and hematite standard EELS spectra was reported after 3 channel spectrum averaging.

Conflicts of interest

The authors declare no conflict of interest.

Acknowledgements

This work is funded by the National Science Foundation CAREER award (DMR-1564950). R. Shahbazian-Yassar's contribution is supported by NSF DMR-1710049. This work made use of instruments in the Electron Microscopy Core of UIC's Research Resources Centre. The UIC JEOL JEM-ARM200CF is supported by an MRI-R2 grant from the National Science Foundation (Grant No. DMR-0959470). The authors acknowledge the UIC Research Resource Centre for providing instrumental support. GLC SAED work made use of the EPIC facility of Northwestern University's NUANCE Centre, which has received support from the Soft and Hybrid Nanotechnology Experimental (SHyNE) Resource (NSF ECCS-1542205), the MRSEC program (NSF DMR-1720139) at the Materials Research Centre, the International Institute for Nanotechnology (IIN), the Keck Foundation, and the State of Illinois, through the IIN.

References

1 P. M. Harrison and P. Arosio, The ferritins: molecular properties, iron storage function and cellular regulation, *Biochim. Biophys. Acta*, 1996, **1275**, 161–162.
2 P. M. Harrison, F. A. Fischbach, T. G. Hoy and G. H. Haggis, Ferric oxyhydroxide core of ferritin, *Nature*, 1967, **216**, 1188–1190.
3 J. M. Williams, D. P. Danson and C. Janot, A Mossbauer determination of the iron core particle size distribution in ferritin, *Phys. Med. Biol.*, 1978, **23**, 001.
4 N. Galvez, *et al.*, Comparative structural and chemical studies of ferritin cores with gradual removal of their iron contents, *J. Am. Chem. Soc.*, 2008, **130**, 8062–8068.
5 J. Hwang, *et al.*, A short Fe-Fe distance in peroxodiferric ferritin: control of Fe substrate versus cofactor decay?, *Science*, 2000, **287**, 122–125.
6 D. J. Smith, Ultimate resolution in the electron microscope?, *Mater. Today*, 2008, **11**, 30–38.
7 A. R. Muir, The molecular structure of isolated and intracellular ferritin, *Q. J. Exp. Physiol. Cogn. Med. Sci.*, 1960, **45**, 192–201.
8 C. Quintana, J. M. Cowley and C. Marhic, Electron nanodiffraction and high-resolution electron microscopy studies of the structure and composition of physiological and pathological ferritin, *J. Struct. Biol.*, 2004, **147**, 166–178.
9 Y. H. Pan, *et al.*, 3D morphology of the human hepatic ferritin mineral core: New evidence for a subunit structure revealed by single particle analysis of HAADF-STEM images, *J. Struct. Biol.*, 2009, **166**, 22–31.
10 Y. H. Pan, *et al.*, Electron-beam-induced reduction of Fe3+ in iron phosphate dihydrate, ferrihydrite, haemosiderin and ferritin as revealed by electron energy-loss spectroscopy, *Ultramicroscopy*, 2010, **110**, 1020–1032.
11 J. L. L. Farrant, AN Electron Microscopic Study of Ferritin, *Biochim. Biophys. Acta*, 1937, **13**, 569–576.

12 W. H. Massover and J. M. Cowley, The Ultrastructure of Ferritin Macromolecules. The Lattice Structure of the Core Crystallites, *Proc. Natl. Acad. Sci. U. S. A.*, 1973, **70**, 3847–3851.
13 J. M. Cowley, D. E. Janney, R. C. Gerkin and P. R. Buseck, The structure of ferritin cores determined by electron nanodiffraction, *J. Struct. Biol.*, 2000, **131**, 210–216.
14 C. Quintana, *et al.*, Initial studies with high resolution TEM and electron energy loss spectroscopy studies of ferritin cores extracted from brains of patients with progressive supranuclear palsy and Alzheimer disease, *Cell. Mol. Biol.*, 2000, **46**, 807–820.
15 C. Quintana, N. Bonnet, A. Y. Jeantet and P. Chemelle, Crystallographic study of the ferritin molecule: new results obtained from natural crystals in situ (mollusc oocyte) and from isolated molecules (horse spleen), *Biol. Cell*, 1987, **59**, 247–254.
16 Y. Pan, *et al.*, Electron beam damage studies of synthetic 6-line ferrihydrite and ferritin molecule cores within a human liver biopsy, *Micron*, 2006, **37**, 403–411.
17 C. C. Calvert, A. Brown and R. Brydson, Determination of the local chemistry of iron in inorganic and organic materials, *J. Electron Spectrosc. Relat. Phenom.*, 2005, **143**, 173–187.
18 C. Wang, Q. Qiao, T. Shokuhfar and R. F. Klie, High-resolution electron microscopy and spectroscopy of ferritin in biocompatible graphene liquid cells and graphene sandwiches, *Adv. Mater.*, 2014, **26**, 3410–3414.
19 W. H. Massover, Ultrastructure of ferritin and apoferritin: A review, *Micron*, 1993, **24**, 389–437.
20 N. D. Jonge and F. M. Ross, Electron microscopy of specimens in liquid, *Nat. Nanotechnol.*, 2011, **6**, 695–704.
21 D. B. Peckys and N. De Jonge, Visualizing gold nanoparticle uptake in live cells with liquid scanning transmission electron microscopy, *Nano Lett.*, 2011, **11**, 1733–1738.
22 T. Murai, *et al.*, Low Cholesterol Triggers Membrane Microdomain-dependent CD44 Shedding and Suppresses Tumor Cell Migration, *J. Biol. Chem.*, 2011, **286**, 1999–2007.
23 D. B. Peckys, P. Mazur, K. L. Gould and N. De Jonge, Fully hydrated yeast cells imaged with electron microscopy, *Biophys. J.*, 2011, **100**, 2522–2529.
24 S. M. Hoppe, D. Y. Sasaki, A. N. Kinghorn and K. Hattar, *In situ* Transmission Electron Microscopy of Liposomes in an Aqueous Environment, *Langmuir*, 2013, **29**, 9958–9961.
25 E. Kennedy, E. M. Nelson, T. Tanaka, J. Damiano and G. Timp, Live Bacterial Physiology Visualized with 5 nm Resolution Using Scanning Transmission Electron Microscopy, *ACS Nano*, 2016, **10**, 2669–2677.
26 J. E. Evans and N. D. Browning, Enabling direct nanoscale observations of biological reactions with dynamic TEM, *J. Electron Microsc.*, 2013, **62**, 147–156.
27 J. E. Evans, *et al.*, Visualizing macromolecular complexes with in situ liquid scanning transmission electron microscopy, *Micron*, 2012, **43**, 1085–1090.
28 J. M. Yuk, *et al.*, High-Resolution Em of Colloidal Nanocrystal Growth Using Graphene Liquid Cells, *Science*, 2012, **336**, 61–64.
29 C. Wang, T. Shokuhfar and R. F. Klie, Precise In Situ Modulation of Local Liquid Chemistry via Electron Irradiation in Nanoreactors Based on Graphene Liquid Cells, *Adv. Mater.*, 2016, **28**, 7716–7722.
30 H. Cho, *et al.*, The Use of Graphene and Its Derivatives for Liquid-Phase Transmission Electron Microscopy of Radiation-Sensitive Specimens, *Nano Lett.*, 2017, **17**, 414–420.
31 J. D. López-Castro, *et al.*, A new approach to the ferritin iron core growth: influence of the H/L ratio on the core shape, *Dalton Trans.*, 2012, **41**, 1320–1324.
32 G. C. Ford, *et al.*, Ferritin: Design and Formation of an Iron-Storage Molecule, *Philos. Trans. R. Soc., B*, 1984, **304**, 551–565.
33 F. A. Fischbach, P. M. Harrison and T. G. Hoy, The structural relationship between ferritin protein and its mineral core, *J. Mol. Biol.*, 1969, **39**, 235–238.
34 N. Jian, M. Dowle, R. D. Horniblow, C. Tselepis and R. E. Palmer, Morphology of the ferritin iron core by aberration corrected scanning transmission electron microscopy, *Nanotechnology*, 2016, **27**, 46.
35 M. Mehlenbacher, *et al.*, Iron Oxidation and Core Formation in Recombinant Heteropolymeric Human Ferritins, *Biochemistry*, 2017, **56**, 3900–3912.
36 N. D. Chasteen and P. M. Harrison, Mineralization in ferritin: an efficient means of iron storage, *J. Struct. Biol.*, 1999, **126**, 182–194.
37 R. M. Cornell and U. Schwertmann, *The Iron Oxides: Structure, Properties, Reactions, Occurrences and Uses*, Wiley, 2006.
38 L. Lajaunie, F. Boucher, R. Dessapt and P. Moreau, Quantitative use of electron energy-loss spectroscopy Mo-M2,3 edges for the study of molybdenum oxides, *Ultramicroscopy*, 2015, **149**, 1–8.
39 T. G. Sparrow, B. G. Williams, C. N. R. Rao and M. J. Thomas, L3/L2 White Line Intensity Ratios in the Electron Energy- Loss Spectra of 3d Transition Metal Oxides, *Chem. Phys. Lett.*, 1984, **108**, 547–550.
40 J. Graetz, C. C. Ahn, H. Ouyang, P. Rez and B. Fultz, White lines and d-band occupancy for the 3d transition-metal oxides and lithium transition-metal oxides, *Phys. Rev. B: Condens. Matter Mater. Phys.*, 2004, **69**, 235103.
41 S. Das, M. J. Hendry and J. Essilfie-Dughan, Transformation of Two-Line Ferrihydrite to Goethite and Hematite as a Function of pH and Temperature, *Environ. Sci. Technol.*, 2011, **45**, 268–275.
42 U. Schwertmann, J. Friedl and H. Stanjek, From Fe(III) ions to ferrihydrite and then to hematite, *J. Colloid Interface Sci.*, 1999, **209**, 215–223.
43 C. Quintana, *et al.*, Study of the localization of iron, ferritin, and hemosiderin in Alzheimer's disease hippocampus by analytical microscopy at the subcellular level, *J. Struct. Biol.*, 2006, **153**, 42–54.

44 Y. Gossuin, R. N. Muller and P. Gillis, Relaxation induced by ferritin: A better understanding for an improved MRI iron quantification, *NMR Biomed.*, 2004, **17**, 427–432.
45 S. V. Yurtaeva, *et al.*, Magnetic Resonance of Ferritin Crystalline Particles in Tumor Tissue, *Appl. Magn. Reson.*, 2012, **42**, 299–311.
46 M. Koralewski, *et al.*, Magnetic birefringence study of the magnetic core structure of ferritin, *Acta Phys. Pol., A*, 2012, **121**, 1237–1239.
47 F. Brem, G. Stamm and A. M. Hirt, Modeling the magnetic behavior of horse spleen ferritin with a two-phase core structure, *J. Appl. Phys.*, 2006, **99**, 123906.
48 L. Yang, C. I. Steefel, M. A. Marcus and J. R. Bargar, Kinetics of Fe(II)-catalyzed transformation of 6-line ferrihydrite under anaerobic flow conditions, *Environ. Sci. Technol.*, 2010, **44**, 5469–5475.
49 J. J. De Yoreo, In-situ liquid phase TEM observations of nucleation and growth processes, *Prog. Cryst. Growth Charact. Mater.*, 2016, **62**, 69–88.
50 Y. Goto, M. Paterson and I. Listowsky, Iron uptake and regulation of ferritin synthesis by hepatoma cells in hormone-supplemented serum-free media, *J. Biol. Chem.*, 1983, **258**, 5248–5255.
51 V. J. Wade, *et al.*, Influence of site-directed modifications on the formation of iron cores in ferritin, *J. Mol. Biol.*, 1991, **221**, 1443–1452.
52 J. Park, *et al.*, Direct Observation of Wet Biological Samples by Graphene Liquid Cell Transmission Electron Microscopy, *Nano Lett.*, 2015, **15**, 4737–4744.
53 X. Wang, J. Yang, C. M. Andrei, L. Soleymani and K. Grandfield, Biomineralization of calcium phosphate revealed by in situ liquid-phase electron microscopy, *Commun. Chem.*, 2018, **1**, 80.
54 J. Hermannsdörfer, N. De Jonge and A. Verch, Electron beam induced chemistry of gold nanoparticles in saline solution, *Chem. Commun.*, 2015, **51**, 16393–16396.
55 K. Haider, L. Wickstrom, S. Ramsey, M. K. Gilson and T. Kurtzman, Enthalpic Breakdown of Water Structure on Protein Active-Site Surfaces, *J. Phys. Chem. B*, 2016, **120**, 8743–8756.
56 J. H. Paterson and O. L. Krivanek, Elnes of 3d transition-metal oxides, *Ultramicroscopy*, 1990, **32**, 319–325.
57 Y. Levy and J. N. Onuchic, Water Mediation in Protein Folding and Molecular Recognition, *Annu. Rev. Biophys. Biomol. Struct.*, 2006, **35**, 389–415.
58 B. Halle, Biomolecular cryocrystallography: Structural changes during flash-cooling, *Proc. Natl. Acad. Sci. U. S. A.*, 2004, **101**, 4793–4798.
59 N. M. Schneider, *et al.*, Electron-Water interactions and implications for liquid cell electron microscopy, *J. Phys. Chem. C*, 2014, **118**, 22373–22382.
60 J. M. Yuk, J. Park, P. Ercius, K. Kim, D. J. Hellebusch, M. F. Crommie, J. Y. Lee, A. Zettl and A. P. Alivisatos, High-resolution EM of colloidal nanocrystal growth using graphene liquid cells, *Science*, 2012, **226**, 61–64.
61 J. Park, V. P. Adiga, A. Zettl, A. Paul Alivisatos and A. P. Alivisatos, High Resolution Imaging in the Graphene Liquid Cell, in *Liquid Cell Electron Microscopy (Advances in Microscopy and Microanalysis)*, ed. F. Ross, Cambridge University Press, 2016, pp. 393–407, DOI: 10.1017/9781316337455.020.
62 W. Regan, *et al.*, A direct transfer of layer-area graphene, *Appl. Phys. Lett.*, 2010, **96**, 2008–2011.
63 L. A. J. Garvie and P. R. Buseck, Ratios of ferrous to ferric iron from nanometre-sized areas in minerals, *Nature*, 1998, **396**, 667–670.

